



The trifunctional electrocatalytic activity of hierarchically structured porous carbon derived from environmentally malignant *Prosopis juliflora*

Sathyanarayanan Shanmugapriya^{a,1}, Mariappan Ganeshbabu^{a,1}, Subramani Surendran^a, Yun Sung Lee^b, Ramakrishnan Kalai Selvan^{a,*}

^a Energy Storage and Conversion Devices Laboratory, Department of Physics, Bharathiar University, Coimbatore, 641046, Tamil Nadu, India

^b Faculty of Applied Chemical Engineering, Chonnam National University, Gwangju, 500-757, South Korea

ARTICLE INFO

Key Words:

Prosopis juliflora
Hydrothermal method
Electrocatalyst
ORR
HER

ABSTRACT

Finding an efficient and affordable multifunctional electrocatalyst with long-term durability has received paramount interest in the recent scenario. The present work attempted to facilitate ecologically threatful invasive biomass – *P. juliflora*- derived porous carbon as an effectual Pt support for trifunctional electrocatalytic applications. The preparation of Pt decorated *P. juliflora*-derived porous carbon (Pt/J-600, Pt/J-700, and Pt/J-800) involves simple hydrothermal carbonization, pyrolysis at various temperatures of 600, 700 & 800°C and polyol mediated reduction. The obtained XRD results reveal the turbostratic nature of the prepared porous carbon favoring to anchor the Pt NPs. Significantly, the estimated I_D/I_G ratios of Raman profile substantiates the highly defective structure of Pt/J-800. The TEM images disclose the agglomeration-free dispersion of Pt NPs in the Pt/J-800 electrocatalyst. The EIS analysis demonstrates the relatively low solution and charge transfer resistances ($R_s = 0.646 \, \Omega$ & $R_{ct} = 0.312 \, \Omega$). The desirable 4e⁻ transfer with an improved limiting current density of $-4.44 \, \text{mA cm}^{-2}$ signpost better oxygen reduction reaction (ORR) performance of Pt/J-800 than the other prepared electrocatalysts. Additionally, the high electrochemical surface area ($652.72 \, \text{m}^2 \text{g}^{-1}$) and good mass activity ($49.09 \, \text{mA mg}_{\text{Pt}}^{-1}$) prove the excellent methanol oxidation reaction (MOR) activity. Moreover, a minimal overpotential of 31 mV @ $10 \, \text{mA/cm}^2$, and a lower Tafel slope of 32 mV/dec with 24 hr stable performance proved the efficient hydrogen evolution reaction (HER) performance of Pt/J-800. The remarkable electrochemical performance of Pt/J-800 is attributed to the enhanced surface area created by hierarchically porous carbon support and the uniform dispersion of Pt nanoparticles with optimum loading.

1. Introduction

Developing clean and renewable energy technologies is crucial for reducing dependence on fossil fuels and addressing environmental challenges. Among the various materials available, carbon-based materials have garnered significant attention due to their versatility in energy storage and conversion applications, with their tunable porosity, high electronic conductivity, and exceptional chemical stability [1,2]. Biomass-derived carbon is a highly desirable option due to its abundance, renewable nature, and ease of processing, making it a sustainable material choice for energy-related applications [3,4]. Every year, over 140 billion metric tons of biomass waste, primarily from agricultural residues, are generated globally. Unfortunately, much of this biomass is

burned, contributing to air pollution and greenhouse gas emissions [5]. The large daily production of lignocellulose biomass, like plant and animal matter, contributes to greenhouse gas emissions, creates waste management challenges, and other environmental impacts [6,7]. Converting these abundant carbon-rich materials into valuable products for energy applications remains a significant challenge in the scientific field.

One of the promising strategies for utilizing biomass waste is the preparation of activated carbon (AC), known for its highly porous structure and exceptionally high specific surface area (up to $3000 \, \text{m}^2 \text{g}^{-1}$) [8–10]. Key characteristics for carbon support in electrocatalytic applications include a high specific surface area to maximize the exposure of active sites, surface defects that effectively anchor and disperse metal nanoparticles (NPs), enriched porosity to promote mass transport,

* Corresponding author.

E-mail address: selvankram@buc.edu.in (R.K. Selvan).

¹ Both the authors have equal contribution.

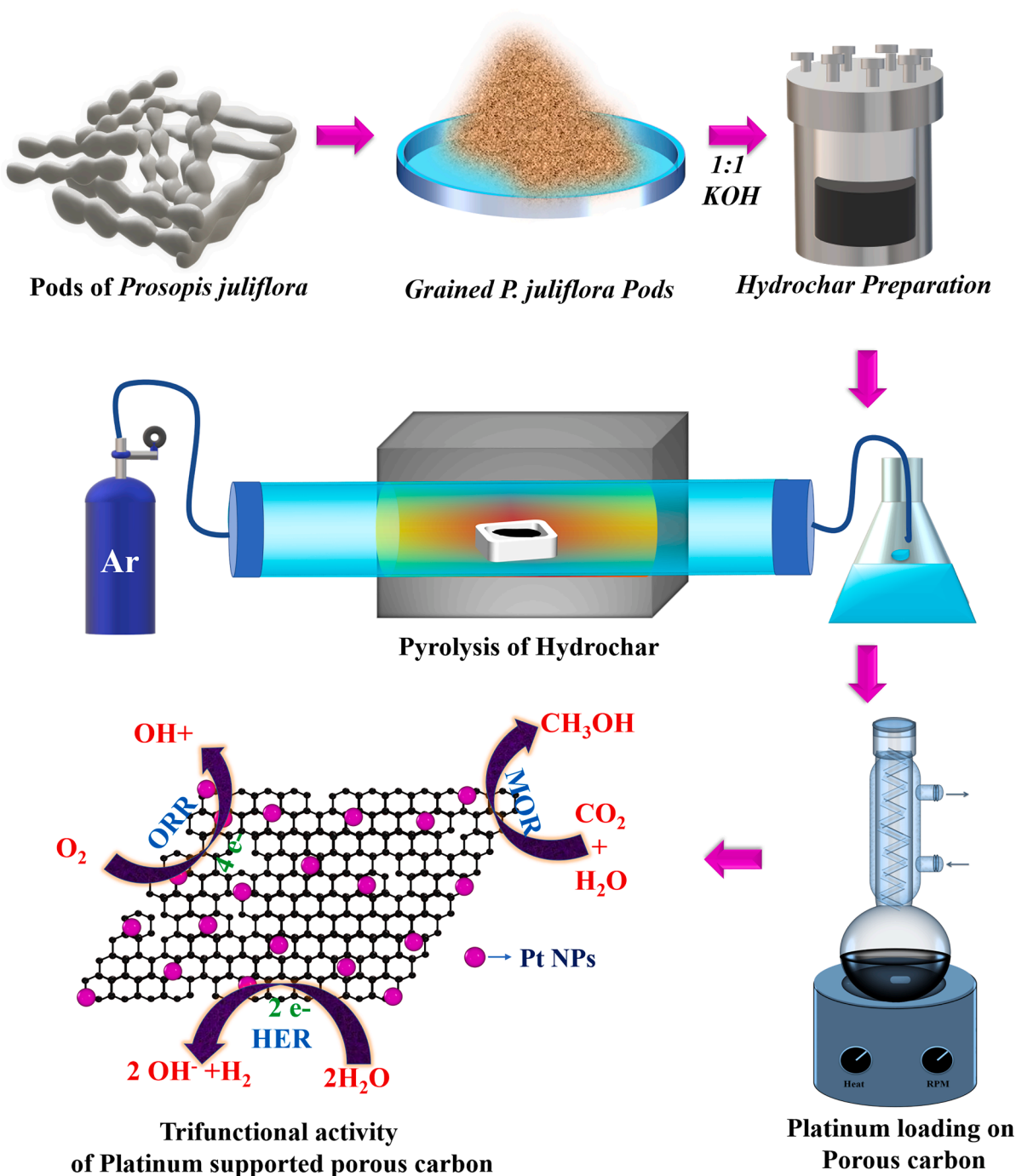


Fig. 1. Schematic representation of Pt decorated *P. juliflora* derived porous carbon synthesis.

and excellent electrical conductivity to ensure efficient electron transfer [11]. Given these attributes, biomass-derived AC is an ideal candidate as a support material for metal NPs in energy conversion technologies such as fuel cells, water electrolysis, and metal-air batteries.

Several studies have demonstrated the potential of biomass-derived carbons as efficient electrocatalyst supports. Yang et al. synthesized carbon from amaranth biomass for hydrogen evolution (HER) and oxygen evolution reactions (OER) that achieved an overpotential of 265 mV for HER and 514 mV for OER at 10 mA/cm² [12]. Hoang et al. developed Ni- and P-doped carbon from waste carrots, showing an overpotential of 368 and 297 mV at 10 mA cm⁻² for OER and HER [13]. Additionally, Hiroshi et al. reported the synthesis of carbon alloy from blood meal and ascidian-derived cellulose nanofibers for OER and ORR

reactions. The blood meal naturally contains pyridine groups (Fe-N₄), which favored the overall oxygen electrode activity of $\Delta E = 936$ mV ($\Delta E = E_{j=10(OER)} - E_{half(ORR)}$) [14]. Guijun Li et al. likely synthesized a Fe-C-CG electrocatalyst from carbon, iron chloride, and coffee grounds, achieving higher ORR activity with improved half-wave potential and a power density in a Zn-air battery [15]. These works highlight the growing interest in utilizing biomass-derived carbons for various energy applications.

Prosopis juliflora (*P. juliflora*), an invasive species, has severely impacted large areas of arable land, disrupting agriculture, water resources, and biodiversity [16,17]. Eradication through burning is not a viable solution due to the associated environmental issues such as greenhouse gas emissions and land degradation. An alternative and

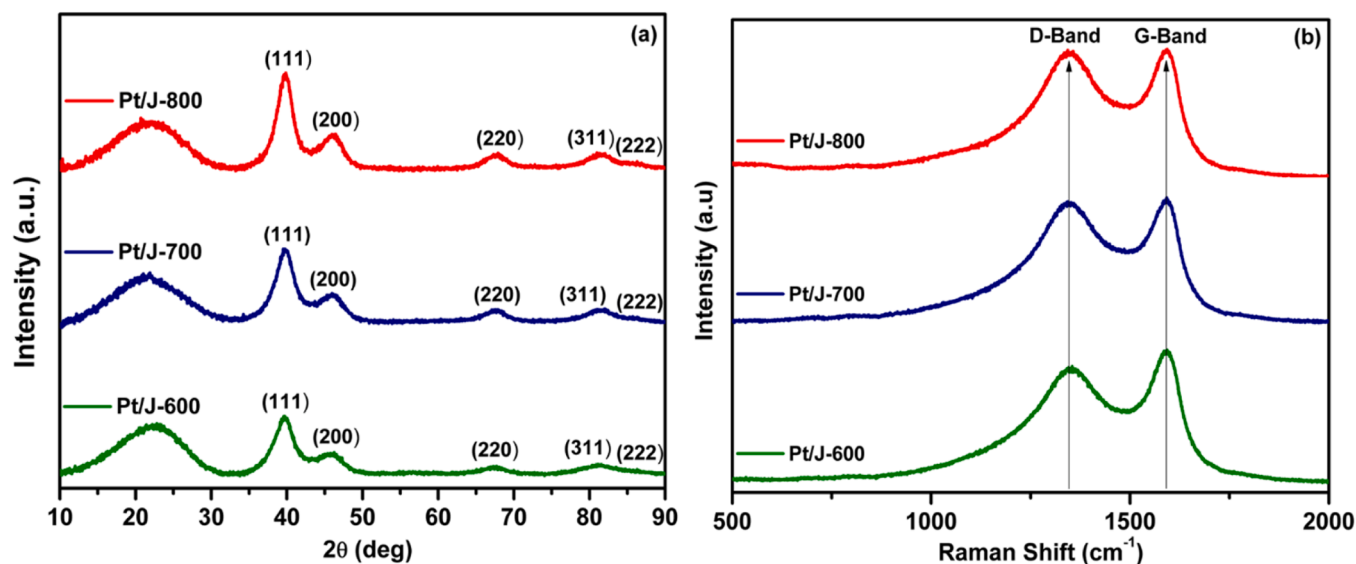


Fig. 2. a) XRD patterns, and b) Raman spectra of Pt/J-600, 700, and 800.

more sustainable approach is to convert this invasive species into a valuable product. *P. juliflora* is a rich source of lignocellulosic biomass, and its abundant pods, with a potential yield of up to 90 kg annually from a single 10-year-old plant, make it an ideal candidate for carbonization. In India, the production of *P. juliflora* pods has been estimated to be two million tonnes per year, indicating the vast availability of raw material for energy applications [18].

The current study explores the development of hierarchically porous carbon support derived from *P. juliflora* pods as a low-cost, sustainable material for electrocatalysis [19]. A polyol-mediated reduction process was employed to prepare platinum (Pt)-loaded porous carbon electrocatalysts (Pt/J = Pt/J-600, Pt/J-700, and Pt/J-800), with variations in the carbonization temperatures. The physicochemical properties of these materials, including structure, surface area, and porosity, were characterized using techniques such as X-ray diffraction (XRD), Raman spectroscopy, X-ray photoelectron spectroscopy (XPS), transmission electron microscopy (TEM), and high-resolution TEM (HRTEM). The electrocatalytic activity of the prepared Pt/J materials was assessed for trifunctional electrochemical applications, specifically the oxygen reduction reaction (ORR), methanol oxidation reaction (MOR), and hydrogen evolution reaction (HER). Among the prepared electrocatalysts, Pt/J-800, carbonized at 800 °C, exhibited superior performance in all electrochemical studies compared to its counterparts. The combination of *P. juliflora*-derived porous carbon and Pt nanoparticles provided excellent catalytic activity, enhanced stability, and improved electron transport. This innovative "waste-to-wealth" approach demonstrates the potential of converting an invasive weed into a valuable electrode material for sustainable energy conversion applications.

2. Experimental methods and materials

2.1. Materials

In this study, the following high-purity AR-grade chemicals were used. Chloroplatinic acid (H_2PtCl_6), Methanol (CH_3OH), Nafion ($\text{C}_7\text{HF}_{13}\text{O}_5\text{S}\cdot\text{C}_2\text{F}_4$), Polyvinylidene fluoride, and N-methyl-2-pyrrolidone (NMP) were obtained from Sigma-Aldrich (USA). Ethylene glycol (EG), Dimethylformamide (DMF), Formaldehyde (HCHO), Potassium hydroxide (KOH), Sodium hydroxide (NaOH), Hydrochloric acid (HCl), Sulphuric acid (H_2SO_4), Absolute ethanol ($\text{CH}_3\text{CH}_2\text{OH}$), and Isopropyl alcohol ($\text{CH}_3\text{CHOHCH}_3$) were obtained from Himedia Laboratories Pvt. Ltd. Commercial Pt/C (20 wt% Pt on Vulcan XC72 Carbon) was purchased from Sainergy Fuel Cell India Pvt. Ltd. The pods of *Prosopis*

juliflora (Biomass) were collected from *P. juliflora* trees in the dried water body of Sathyamangalam town (11.5048° N, 77.2384° E) in Tamil Nadu, India.

2.2. Synthesis of Pt-decorated *P. juliflora*-derived porous carbon

The protocol for synthesizing Pt-decorated *P. juliflora* derived porous carbon is given schematically in Fig. 1. For the typical synthesis [19], the desired amount (2 g) of well-dried and ground pods of *P. juliflora* was hydrothermally treated with 1 M H_2SO_4 at 180 °C for 24 hr. The obtained hydrochar was activated with KOH (1:1 wt ratio) followed by pyrolysis at 600 °C, 700 °C, and 800 °C for 1 hr under an Ar atmosphere with a heating rate of 10 °C. min⁻¹. The obtained material was thoroughly washed with dil. HCl, water, and ethanol until neutral pH was reached. A simple polyol-mediated formaldehyde reduction method was adopted for 5wt% Platinum loading on the prepared porous carbon [20–22]. The prepared Pt-decorated material was labeled as Pt/J-600, Pt/J-700, and Pt/J-800.

2.3. Physicochemical studies

The XRD pattern and Raman spectra were obtained using a Rigaku D/Max 2400 X-ray diffractometer (Japan) with Cu K α radiation and HORIBA Jobin Yvon LabRAM HR 800, respectively. The XPS analysis was carried out with a SPECS FlexMod (Germany) using a Kratos Analytical spectrometer. The surface morphology of the prepared materials was analyzed by TEM analysis using the JEOL JEM 2100 and Hitachi HF-3300 high-resolution transmission electron microscopes.

2.4. Electrochemical measurements and electrode preparation

The standard three-electrode system is used to study the electrocatalytic properties of the materials. The modified glassy carbon electrode (diameter: 3 mm, area: 0.0706 cm²) was used for MOR and ORR studies with the catalyst loading of 5 μL . In this regard, 4 mg of active material was dispersed in 100 μL of isopropyl alcohol, 300 μL of deionized water, and 8 μL of 5 wt% Nafion solution. The ORR activity was studied using RDE and RRDE techniques. On the other hand, the pre-treated flexible carbon cloth (1 × 1 cm², 0.5 mm) is used as the substrate for HER analysis, where the prepared homogeneous slurry (80:10:10 ratio of active material: carbon black: PVDF in NMP solution) was brush coated and dried at 80 °C for overnight in a vacuum oven. Pt coil and Ag/AgCl were used as counter and reference electrodes,

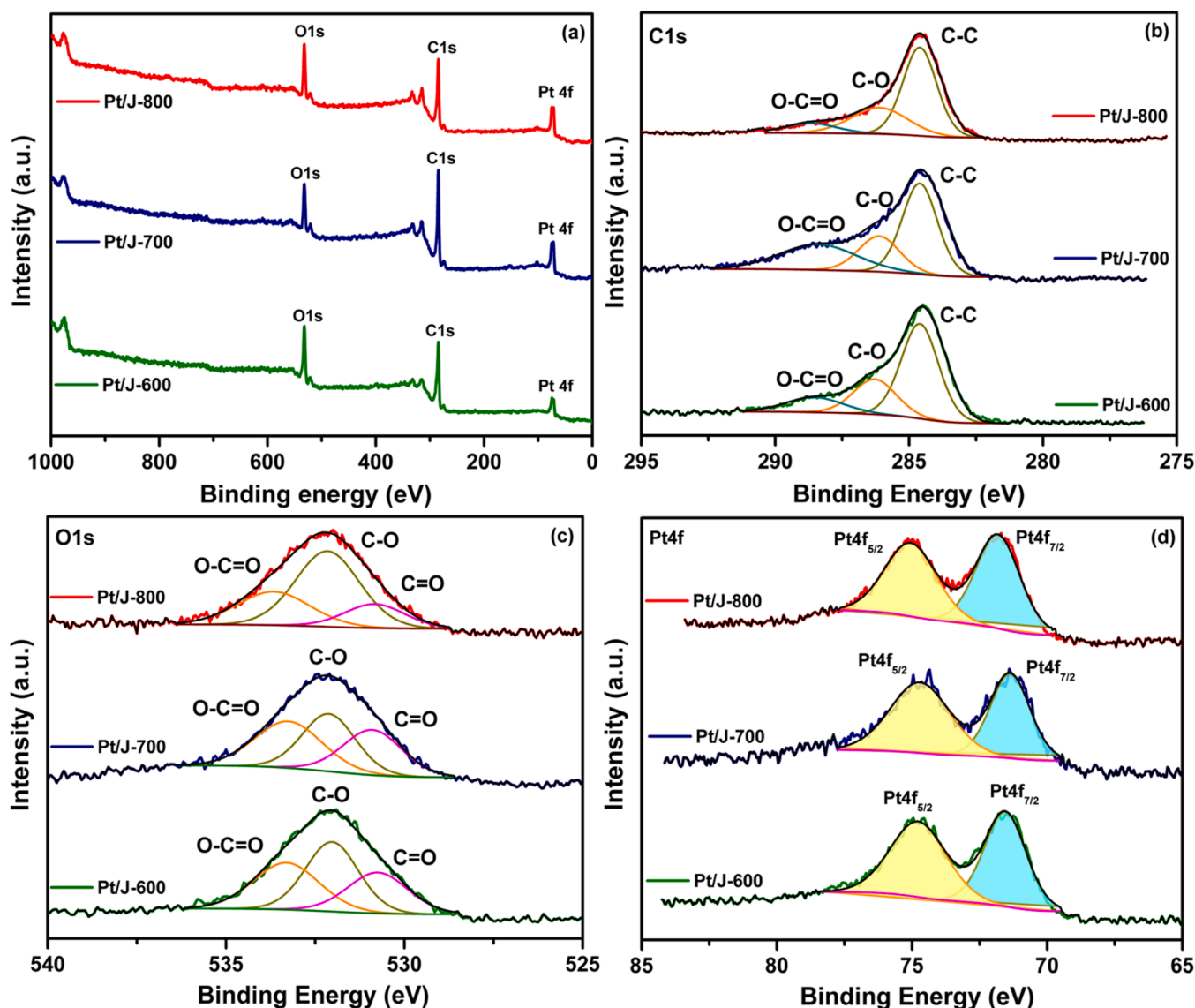


Fig. 3. a) XPS Survey, b) C 1 s, O 1 s, and Pt 4f spectra of Pt/J-600, 700, 800.

respectively. The electrochemical impedance spectroscopy of the present work was carried out using the SP-150 single channel, and all the other electrochemical techniques are done with VSP-Multichannel potentiostat of Bio-Logic Science Instruments.

3. Results and discussion

3.1. Physicochemical properties of Pt/Js

Fig. 2a shows the XRD patterns of prepared Pt/J-600, Pt/J-700, and Pt/J-800 electrocatalysts. It shows all three samples exhibited a similar XRD pattern. The observed broad peak around 23° infers the (002) plane of carbon. The calculated d-spacing (0.39 nm) is higher than graphite (~ 0.34 nm), which validates the highly turbostratic nature of the

prepared carbon supports. Moreover, the turbostratic quality of carbon support ensures adequate anchoring sites that lead to significant dispersion of Pt NPs [11]. Similarly, the observed peaks at 39.71° , 46.19° , 67.41° , 81.21° , and 85.65° corresponding to the planes of (111), (200), (220), (311), and (222) infer the formation of face-centered cubic structure of Pt (JCPDS No. 70–2431), respectively. Thus, the XRD results corroborate the reduction of Pt ions into metallic crystal structures and their successful anchoring on prepared hierarchically porous carbon support [23]. Further, the calculated crystallite size using Scherrer's formula is 1.8–2.8 nm.

The degree of graphitization of Pt-loaded carbon was studied using Raman spectra and is shown in Fig. 2b. The prepared Pt/Js display two significant peaks around ~ 1330 cm^{-1} for the D-band and 1590 cm^{-1} for the G-band. The observed D-band confirms the presence of sp^3 defect sites corresponding to the disordered carbon. On the other hand, the G-band infers that the sp^2 -hybridized carbon has an in-plane vibration in a graphite layer that measures graphitized carbon. The calculated intensity ratio of I_D and I_G band renders the degree of graphitization [24]. The estimated I_D/I_G ratios are 0.90, 0.98, and 1.0 for Pt/J-600, 700, and 800, respectively. The observed results confirm the highly defective structure of Pt/J-800 that has originated from the hierarchically porous network of J-800 [23].

Table 1

Elemental composition of Pt/Js obtained from XPS analysis.

Electrocatalysts	C1s	O1s	Pt 4f _{7/2}	Pt 4f _{5/2}
Pt/J-600	79.96	16.97	1.19	1.88
Pt/J-700	77.09	18.35	2.11	2.45
Pt/J-800	73.82	20.84	2.26	3.08

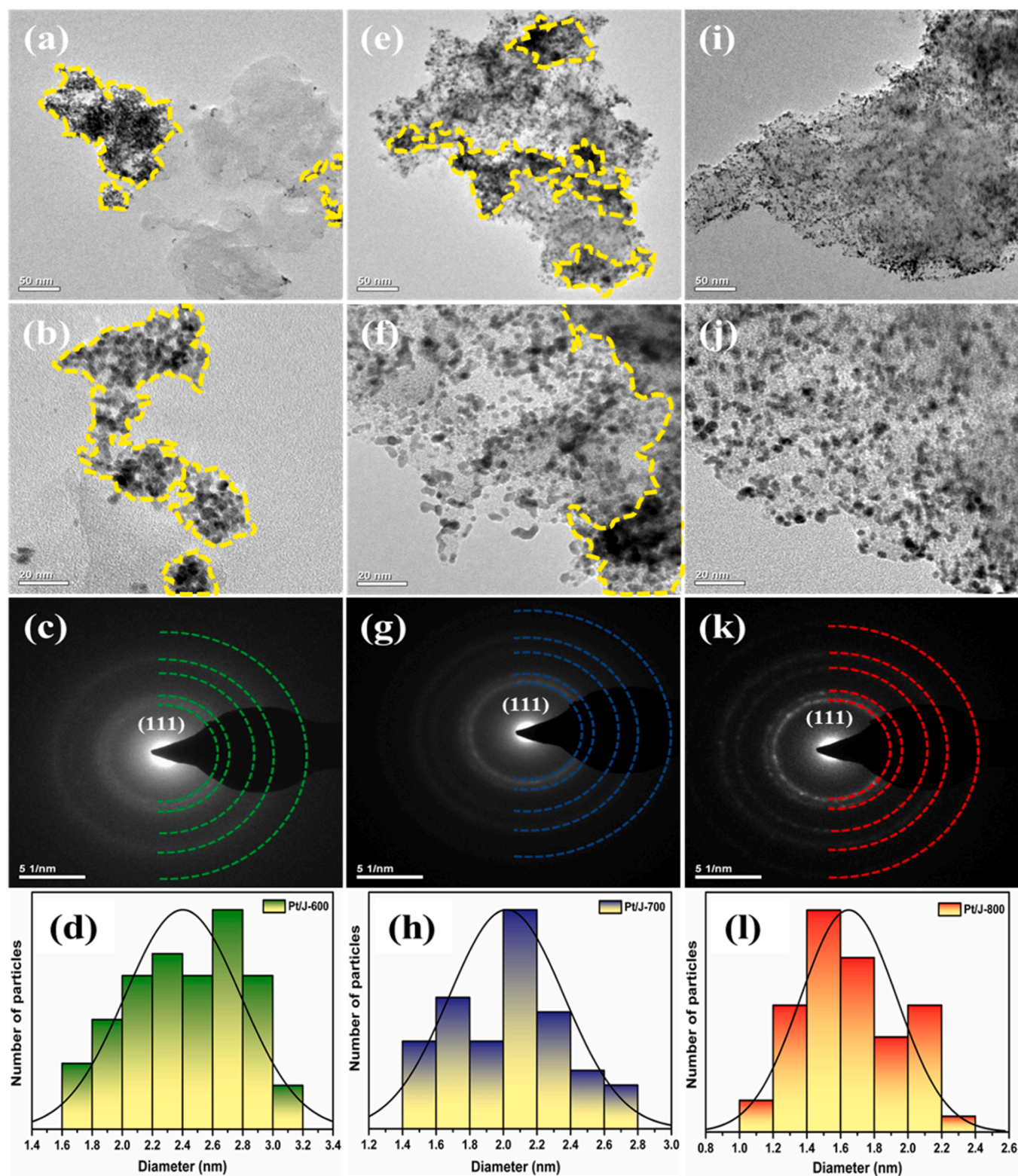


Fig. 4. TEM micrographs, SAED pattern, and particle size histogram of Pt/J-600 (a-d), Pt/J-700 (e-h), and Pt/J-800 (i-l), respectively.

The X-ray photoelectron spectra reveal the surface chemical composition and the oxidation state of Pt in prepared Pt/Js. The survey spectra (Fig. 3a) of Pt/Js exhibit the presence of carbon, oxygen, and platinum elements, and the corresponding atomic percentages are given in Table 1. The increase in the atomic percentage of Pt from Pt/J-600 to Pt/J-800 with identical mass loading validates the significant dispersion of Pt NPs in Pt/J-800. Further, the C 1 s spectra (Fig. 3b) are

deconvoluted at binding energies of 284, 286, and 289 eV corresponding to the aliphatic/aromatic C-C/C=C, hydroxyl C-O, and carbonyl O-C=O carbon, respectively [25,26]. Similarly, the deconvoluted O 1 s spectra (Fig. 3c) ascribed the functional groups of C=O, C-O-C, and O-C=O at the binding energies of 531.02, 532.95, and 533.01 eV, respectively [23]. The Pt 4f signals of the prepared Pt/Js (Fig. 3d) display two significant peaks around 71.8 and 75.5 eV corresponding to the spin-orbital

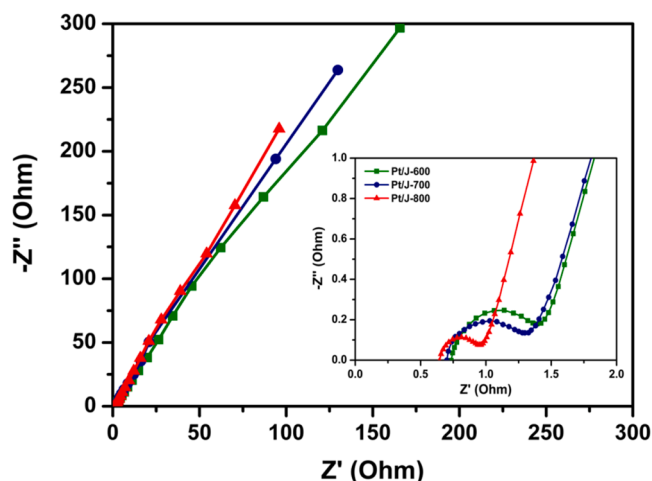


Fig. 5. Electrochemical impedance spectral analysis: Nyquist plots of prepared Pt/Js. Inset: Enlarged view of the obtained Nyquist plots.

splitting of Pt $4f_{7/2}$ and Pt $4f_{5/2}$ states, which infers the metallic Pt(0) [27]. One can see from Table 1 that the amount of O_2 in Pt/J-800 is significantly higher, which is advantageous for catalytic applications. [28,29]

The morphological features, including the dispersion, crystallinity, and size of the Pt NPs, are studied using the transmission electron microscope. Fig. 4 portrays the microscopic depiction of Pt-loaded porous carbon, where the nearly spherical dark spots represent the Pt NPs. Fig. 4a,b shows the poorly oriented and agglomerated dispersion of Pt NPs in Pt/J-600. Besides, the dispersed Pt NPs are not significantly crystalline, exhibiting an obscure form of concentric circles in the obtained SAED pattern (Fig. 4c). The particle size histogram (Fig. 4d) depicting an average size of the particles is 2.4 nm under a standard distribution curve.

The TEM micrograph of Pt/J-700 (Fig. 4e, f) displays a far better dispersion, better crystallinity (Fig. 4g), and a smaller particle size of 2 nm (Fig. 4h) than the Pt/J-600. Interestingly, highly uniform and agglomeration-free dispersion of Pt NPs is observed for Pt/J-800 (Fig. 4i, j). Moreover, the SAED pattern (Fig. 4k) displays a sharp and clear dotted ring-like pattern of concentric circles portraying the crystallinity of the loaded Pt NPs. It corresponds to the lattice planes of (111), (200), (220), (311), and (222) planes of the cubic structure (fcc) of Pt (JCPDS No. 70-2431). Furthermore, the average particle size is around 1.8 nm from Fig. 4l, which is significantly lower than the rest of the samples. Overall, the Pt/J-800 illustrates uniform and dense loading of Pt NPs with fewer particle sizes devoid of undesirable agglomeration. The highly significant Pt loading is attributed to its hierarchical porous network that creates adequate anchoring sites for immobilizing Pt NPs in defects, vacancies, and edges. Moreover, the higher content of oxygen functional groups in Pt/J-800 may also act as nucleation sites to grow Pt NPs [23]. Thus, compared to Pt/J-600 and 700, Pt/J-800 with well-distributed smaller Pt NPs are observed to be advantageous for enhanced electrocatalytic activity.

3.2. Electrocatalytic properties of Pt/Js

3.2.1. Electrochemical impedance spectral (EIS) analysis

Fig. 5 shows the Nyquist plot of prepared Pt/Js electrocatalysts. The EIS analysis is studied from 0.1 MHz to 1 MHz at an open-circuit voltage with a potential amplitude of 10 mV. It is well known that the typical Nyquist plot contains an arc-like pattern in the high-frequency region and a tail-like vertical line in the low-frequency region. The obtained semicircle (Fig. 5 inset) at the high-frequency region describes the pseudo-transfer resistance due to the porous nature of the electrode [30]. The obtained solution resistance (R_s) and charge-transfer

resistance (R_{ct}) are 0.737 Ω and 0.653 Ω for Pt/J-600, 0.707 Ω and 0.601 Ω for Pt/J-700, 0.646 Ω and 0.312 Ω for Pt/J-800, which is calculated from the commencement and the diameter of the semi-circle. The solution resistance comprises contact resistance at the electrode-electrolyte interface, ionic resistance of the electrolyte, and intrinsic resistance of the substrate [24]. In contrast, the charge-transfer resistance depicts the resistance imposed on electron transfer at the interface. Among these, the Pt/J-800 provides significantly lower resistance than the prepared other electrocatalysts. Similarly, the low-frequency region, Pt/J-800, shows an exceedingly vertical-line feature exhibiting low diffusion resistance towards the electrolytic ions. The relatively shorter length of this vertical line implies a faster rate of ion transport into the electrode. Thus, Pt/J-800 displays better electronic conductivity due to its remarkable porous structure, high specific surface area, and good accessibility for electrolytic ions.

3.2.2. Oxygen reduction reaction (ORR) studies

The ORR kinetics of the prepared Pt/Js are studied using a rotating disk electrode (RDE) at various speeds from 300 to 1800 rpm. The obtained LSV polarization curves are shown in Fig. 6(a-c). The kinetic transfer region ($\sim 0.8 - 1 V_{RHE}$), mass transport region ($\sim 0.6 - 0.8 V_{RHE}$), and diffusion control region ($\sim 0.3 - 0.6 V_{RHE}$) are the three separate regions of LSV. For the electrocatalyst Pt/J-800, the diffusion control region starts earlier than other sections. As rotation speed increased, the limiting current in every catalyst rose because the oxygen was more readily available close to the electrode surface. Also, it can be seen that the current density is limited below 0.6 V vs. RHE. Subsequently, the Koutecky-Levich (K-L) plot (Fig. 6(d-f)) is drawn to calculate the number of electrons transferred during ORR using the current density at various potentials of the limiting current region and the inverse of the square root of rotation speed ($\omega^{-1/2}$ vs. J^{-1}) [31]. The K-L plots of prepared Pt/J-600, Pt/J-700, and Pt/J-800 electrocatalysts display linear and parallel characteristics validating the first-order kinetics [32], and the number of electrons transferred during the oxygen reduction is ~ 4 . Fig. 7a shows the RDE polarization curves of Pt/Js and the 20 wt.% commercial Pt/C measured at 1500 rpm for comparison. Three significant parameters, including onset potential, half-wave potential, and limiting current density, are determined from the LSV curves and are given in Fig. 7b and Table 2. Among the prepared electrocatalysts, the Pt/J-800 delivered an early onset potential of 0.95 V_{RHE} , at 0.1 $mA\ cm^{-2}$ than the commercial Pt/C (0.97 V_{RHE}) in the kinetic-current region. Similarly, the calculated half-wave potential in the mixed-kinetic region shows the minimum negative shift of $\Delta E_{1/2} = 30$ mV than the commercial Pt/C (0.85 V_{RHE}). As well as, the limiting-current density of Pt/J-600 ($-3.96\ mA\ cm^{-2}$), Pt/J-700 ($-4.09\ mA\ cm^{-2}$), and Pt/J-800 ($-4.44\ mA\ cm^{-2}$) is higher than the commercial Pt/C ($2.73\ mA\ cm^{-2}$). Also, the mass activity of the prepared electrocatalysts are calculated using the kinetic current densities normalized by mass loading of Pt (30 $\mu g\ cm^{-2}$) and are 2.87, 36.27, and 39.06 $A\ g^{-1}$ for Pt/J-600, 700, and 800, respectively. Overall, Pt/J-800 delivered better catalytic performance in terms of early-onset (0.95 V_{RHE}), relatively positive $E_{1/2}$ (0.86 V_{RHE}), and a maximum limiting-current density ($-4.44\ mA\ cm^{-2}$) than the commercial Pt/C and comparable with the reported Pt-loaded biomass-derived carbon based electrocatalysts (Table 2).

Fig. 7c shows the Tafel plots of the prepared electrocatalysts, which exhibit two different Tafel slopes at the high- and low- overpotential regions, elucidating the potential-dependent reaction mechanism [33]. The obtained Tafel slopes are 98 and 140 $mV\ dec^{-1}$ for Pt/J-600, 86 and 135 $mV\ dec^{-1}$ for Pt/J-700, and 71 and 135 $mV\ dec^{-1}$ for Pt/J-800, which is comparable with the Pt electrocatalysts (60, and 120 $mV\ dec^{-1}$). Thus, the ORR reaction mechanism of the prepared Pt/J electrocatalysts is alleged to follow the dissociative and associative reduction of oxygen at the low-current and high-current regions, respectively [34].

Further, the rotating ring disk electrode (RRDE) analysis is carried out for the Pt/J-800 electrocatalyst (Fig. 7d). The RRDE equipped with a bi-potentiostat monitors both the reduction reaction and intermediate

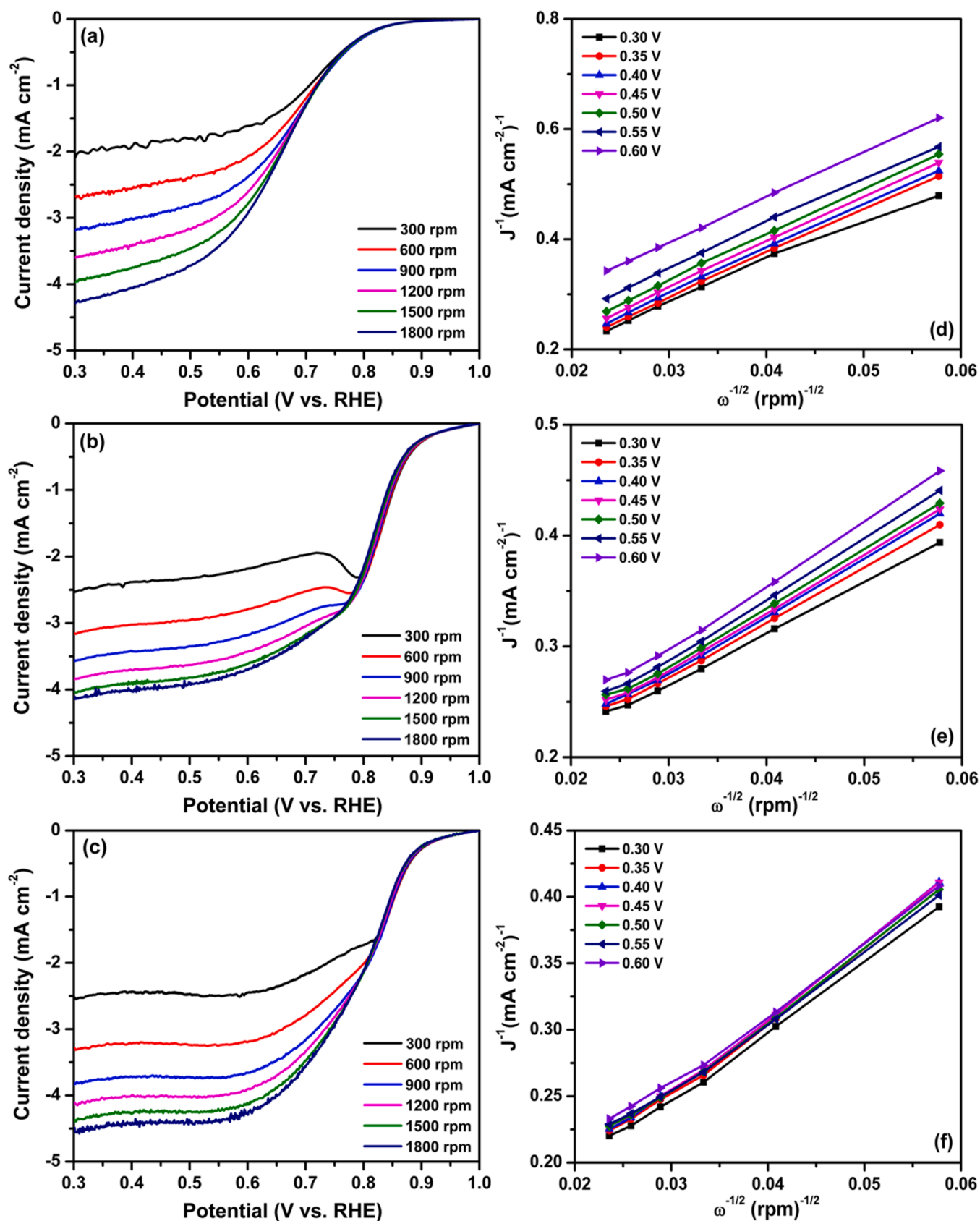


Fig. 6. (a-c) LSV polarization curves measured using RDE at various rotation speeds, and (d-f) corresponding K-L plots of Pt/J-600, Pt/J-700, and Pt/J-800 electrocatalysts, respectively.

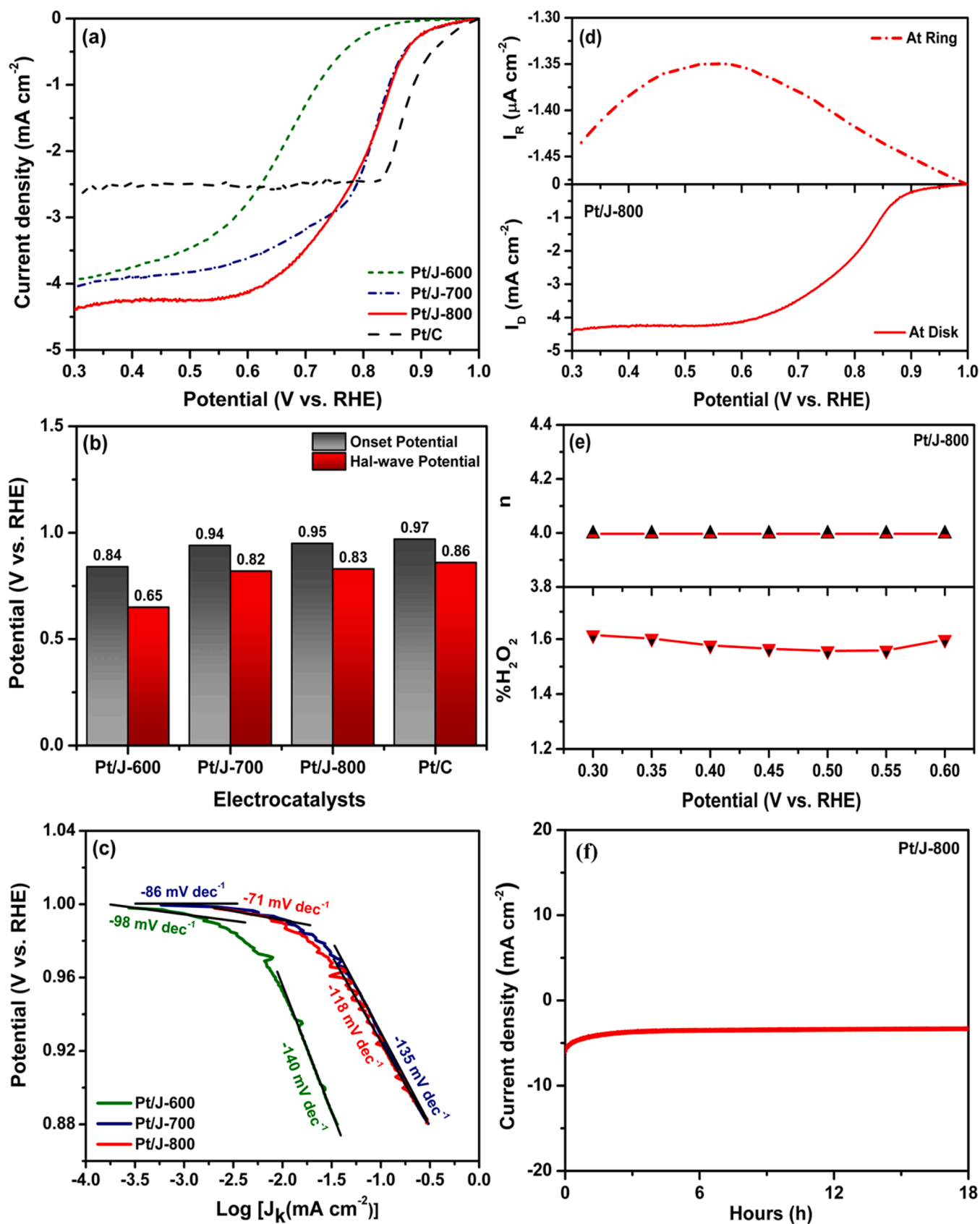


Fig. 7. a) Comparative polarization curves of prepared electrocatalysts at 1500 rpm, b) bar diagram on the onset and half-wave potentials of individual electrocatalysts, c) Tafel plot, d) RRDE measurement of Pt/J-800, e) n and H_2O_2 % of Pt/J-800, and f) chronoamperometry of Pt/J-800.

Table 2

Comparison of ORR catalytic activity of prepared electrocatalysts with other related reports on biomass-derived Pt-loaded electrocatalysts.

ORR Electrocatalysts	Onset Potential (V _{RHE})	Halfwave Potential (V _{RHE})	Limiting- Current Density (mA cm ⁻²)	Mass Activity (At 0.85 V _{RHE}) (mA mg ⁻¹)	Ref
Pt/N-AVC	0.70	0.87	6.15	2.06 (at 0.9 V _{RHE})	[37]
Pt/HTC-Pyr	0.94	NA	~ -5	5.5	[11]
Pt/OP-AC	0.84	NA	~ -1.7	NA	[30]
Pt/MC-800	0.91	NA	~ -5.5	1.39	[38]
Pt/J-600	0.84	0.65	-3.96	2.87	Present Work
Pt/J-700	0.94	0.82	-4.09	36.27	
Pt/J-800	0.95	0.83	-4.44	39.06	

formation simultaneously at the disk and ring electrodes. The recorded currents at the disk and the ring are I_d and I_r , respectively [35]. The obtained microampere ring current infers the insignificant production of undesirable hydrogen peroxide intermediates. Further, the electron

transfer number (n) and the % yield of H_2O_2 during oxygen reduction are calculated in the potential range between 0.6 V_{RHE} and 0.3 V_{RHE} (Fig. 7e) [36]. The assessed 4-electron transfer corroborates the efficient and direct reduction of oxygen to H_2O . As well as, the calculated % of H_2O_2 is trivial, with < 2% substantiating the 4 electron transfer and negligible production of intermediates during ORR [6]. Finally, the chronoamperometry is carried out to investigate the durability of ORR (Fig. 7f) for 18 h under an uninterrupted supply of oxygen at an applied constant voltage of 0.3 V_{RHE}. The Pt/J-800 electrocatalyst underwent the durability test by continuous oxygen reduction with an insignificant decrement in current density.

3.2.3. Methanol oxidation reaction studies

The electrochemical active surface area (ECSA) of the electrocatalyst is calculated using CV analysis (Fig. 8a). The measured cyclic voltammogram in 0.5 M H_2SO_4 at 50 mV s⁻¹ exhibit the adsorption and desorption peak of atomic hydrogen in the potential range of -0.3 to 0 V vs. Ag/AgCl. The ECSA is calculated using the mean value of hydrogen adsorption and desorption coulombic charge (Q_H mC), mass loading of Pt ($M_{Pt} = 30 \mu g cm^{-2}$), and the charge that can oxidize the hydrogen-monolayer adsorbed on a bright Pt surface (0.21 mC) [24,39]. The obtained ECSAs are 22.59 m² g⁻¹ for Pt/J-600, 43.17 m² g⁻¹ for Pt/J-700,

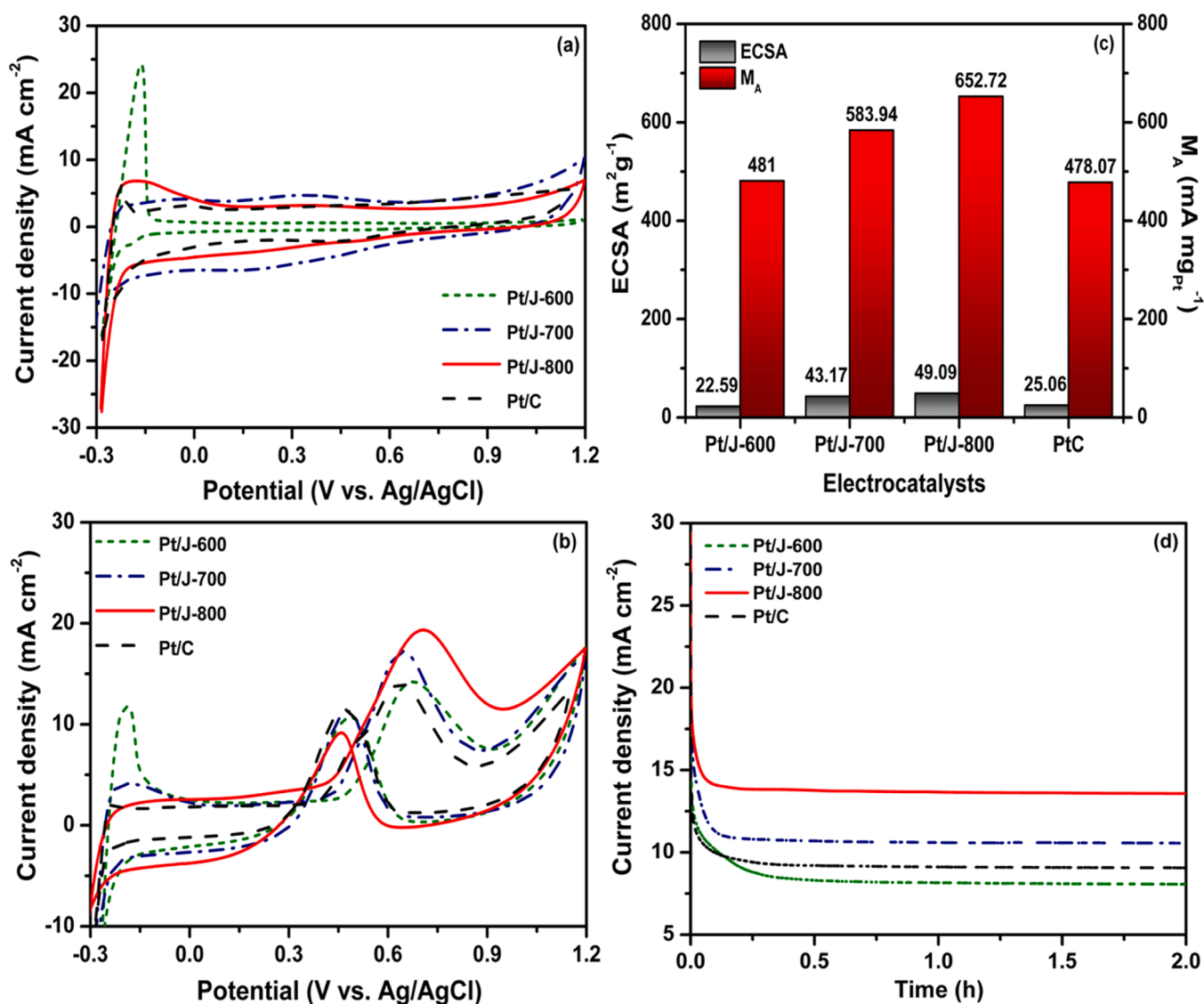


Fig. 8. a) CV curves obtained in 0.5 M H_2SO_4 , b) CV curves obtained in a mixed electrolytic solution of 0.5 M H_2SO_4 +1 M CH_3OH , c) bar diagram illustrating the calculated ECSA and M_A of individual electrocatalysts, d) chronoamperometric response of Pt/J electrocatalysts at 0.65 V_{Ag/AgCl} for 2h

Table 3

Comparison of MOR catalytic activity of prepared electrocatalysts with other related reports on biomass-derived Pt loaded electrocatalysts.

MOR Electrocatalysts	Pt (w. t. %)	Electrolyte	ECSA (m ² g ⁻¹)	I _f /I _b	Mass Activity (A g ⁻¹)	Ref
Pt/HPNC800	13.8	0.5 M	28.99	1.28	211	[23]
Pt/HPNC900	14.4	HClO ₄ + 1	64.1	1.52	721	
Pt/HPNC1000	13.5	M CH ₃ OH	55.1	1.56	613	
PtNWS/CS	NA	0.5 M	55.6	1.2	450	[24]
		H ₂ SO ₄ + 1 M CH ₃ OH				
Pt/MoS ₂ /CNX	5	0.5 M	111.2	NA	1030.2	[25]
Pt/MoS ₂ /C	5	H ₂ SO ₄ + 1 M CH ₃ OH	84.9		710.1	
Pt/CS	NA	0.5 M	NA	0.95	NA	[40]
		H ₂ SO ₄ + 0.5 M CH ₃ OH				
Pt/C-1	20	0.5 M	124.7	0.85	10	[22]
Pt/C-2	20	H ₂ SO ₄ + 0.5 M	58.82	1.52	45	
Pt/C-3	20	0.5 M	261.4	1.59	240	
Pt/C-4	20	CH ₃ OH	68.33	1.5	130	
Pt/ODC	20	0.5 M	58.2	0.86	NA	[41]
		H ₂ SO ₄ + 0.5 M CH ₃ OH				
Pt/NGC	20.2	0.5 M	85.0	NA	201	[42]
Pt/NCA	20.6	H ₂ SO ₄ + 0.5 M	82.6		178	
Pt/NCS	20.8	0.1 M	67.2		168	
		CH ₃ OH				
Pt/NC	20	0.5 M	NA	NA	395	[43]
		H ₂ SO ₄ + 1 M CH ₃ OH				
PRC/BMC	11.3 ± 1.5	0.5 M	16.7	NA	71	[44]
		H ₂ SO ₄ + 0.5 M				
PRC/BTC	(Pt + Cu + Ru)	0.5 M	37.6		228	
		CH ₃ OH				
Pt/J-600	5	0.5 M	22.59	1.32	481	This Work
Pt/J-700		H ₂ SO ₄ + 1	43.17	1.60	583	
Pt/J-800		M CH ₃ OH	49.09	2.10	652	

and 49.09 m² g⁻¹ for Pt/J-800. Overall, Pt/J-800 provides a better ECSA than the other prepared electrocatalysts and 20 wt.% commercial Pt/C (22.06 m² g⁻¹).

Subsequently, the CV analysis is carried out in 0.5 M H₂SO₄ + 1 M CH₃OH to evaluate the methanol oxidizing capability. Fig. 8b shows the CV curves of all the prepared electrocatalysts, which exhibit two anodic peaks in the potential range of 0.4 to 0.9 V_{Ag/AgCl} during the forward scan and 0.6 to 0.2 V_{Ag/AgCl} during the reverse scan. The forward peak represents the oxidation of methanol, which results in the formation of adsorption intermediates, and these intermediates get oxidized during the reverse scan [24]. The early onset and higher forward peak current density (I_f) is essential parameters to compare the performance of the MOR electrocatalysts [24]. However, all the electrocatalysts displayed an identical onset potential of ~0.4 V that comparable with commercial Pt/C (0.38 V). The obtained I_f values are 14.43 mA cm⁻² for Pt/J-600, 17.52 mA cm⁻² for Pt/J-700, and 19.58 mA cm⁻² for Pt/J-800. By normalizing the forward peak current density with mass loading of Pt, the mass activity of the electrocatalysts is calculated [25] and is 481, 583, and 652 A g⁻¹ for Pt/J-600, 700, and 800, respectively (Fig. 8c). Overall, Pt/J-800 delivers a maximum I_f and M_A compared with other electrocatalysts and 20 wt. % Pt/C (14.34 mA cm⁻² and 478 A g⁻¹).

Besides the catalytic activity, anti-poisoning tolerance is essential for evaluating the Pt-based electrocatalysts since the adsorbed carbonaceous intermediates cause the poisoning of Pt catalytic sites. By calculating the I_f/I_b ratio, the anti-poisoning ability can be measured because the reverse peak current density represents the oxidation of such intermediates, and the forward peak current density represents the oxidation of methanol. The calculated I_f/I_b ratios are 1.32, 1.60, and

2.08 for Pt/J-600, Pt/J-700, and Pt/J-800, respectively. The maximum value of I_f/I_b ensures the enhanced anti-poisoning nature of the MOR electrocatalysts [40]. Thus, the anti-poisoning quality of Pt/J-800 is appreciable than the other electrocatalysts and commercial Pt/C (1.23). The prepared Pt/Js electrocatalysts are alleged to follow the conventional reaction mechanism of Pt-based electrocatalysts involving the methanol dehydrogenation controlling the low-potential region followed by oxidation of carbonaceous intermediates (CO_{ads}) being the rate-determining step of the high-potential area [40]. Here, the surface functional groups of the carbon support improve the hydrophilicity, promoting water coordination and dissociation at the Pt catalytic sites, enhancing the generation of mobile -OH species that has a consequential effect on the acceleration of intermediate oxidation. Thus, reducing the poisoning of Pt catalytic sites of Pt/Js electrocatalysts [24].

Subsequently, the chronoamperometric studies are also carried out for Pt/Js and commercial Pt/C. Fig. 8d shows the obtained i-t curves evaluating the stability of electrocatalysts at a constant voltage of 0.65 V for 2 h. Since the potential is set at a constant voltage of methanol oxidation, the intermediate formation also takes place proportionally, resulting in the blockage of Pt catalytic sites and deterioration of catalytic activity. Hence, the decay of current density with respect to time ensures the stability of electrocatalysts [40]. The initial current density of Pt/J-800 is far higher than the other electrocatalysts corroborating its relatively better surface-available active sites. Besides, Pt/J-800 reports comparatively better stability than the other prepared Pt/Js and commercial Pt/C. Table 3 compares the MOR catalytic activity of prepared electrocatalysts and Pt loaded biomass-derived carbon supports.

3.2.4. Hydrogen evolution reaction studies

Fig. 9a shows the LSV polarization curves for hydrogen evolution reactions of Pt/Js electrocatalysts and are studied in 0.5 M H₂SO₄ electrolyte at 5 mV s⁻¹. It can be seen that the Pt/J-800 exhibits an early onset potential comparatively. The overpotentials demanded by the electrocatalysts at 10 mA cm⁻² are 75 mV for Pt/J-600, 60 mV for Pt/J-700, and 31 mV for Pt/J-800 (Fig. 9b). Besides, the calculated mass activity of HER at an overpotential of 200 mV are 2.5, 3.2, and 7.9 A g⁻¹ for Pt/J-600, 700, and 800, respectively. Further, the calculated Tafel slopes (Fig. 9c) are 51 mV dec⁻¹ for Pt/J-600, 45 mV dec⁻¹ for Pt/J-700, and 32 mV dec⁻¹ for Pt/J-800, elucidating the reaction mechanism through the reduction of hydronium ions by following either Volmer-Heyrovsky or Volmer-Tafel pathways. Typically, the Tafel slope values for Volmer, Heyrovsky, and Tafel reaction steps are 120, 40, and 30 mV dec⁻¹ [45]. Based on the obtained Tafel slopes, the Pt/J-600 and Pt/J-700 follow the Volmer-Heyrovsky pathway, whereas the Pt/J-800 electrocatalyst follows the Volmer-Tafel route.

Among the prepared electrocatalysts, Pt/J-800 has displayed relatively better electrocatalytic activity through early-onset potential, a minimal overpotential, higher mass activity, and a low Tafel slope. Moreover, the HER catalytic activity of Pt/J-800 with a minimum metal loading of (5 wt. %) is almost identical to commercial Pt/C (20 wt. %). The measured durability test of Pt/J-800 (Fig. 9d) at -0.1 V_{RHE} for 24 h exhibits continuous evolution of hydrogen gas bubbles throughout the test period, thus displaying enhanced stability with negligible deterioration in the initial current density. Overall, Pt/J-800 electrocatalyst performed well when compared with other carbon supports [46–48].

3.3. Discussion on the enhanced electrocatalytic activity of Pt/J-800

The best electrocatalytic performance of Pt/J-800 among the prepared electrocatalysts, surpassing many equivalent electrocatalysts and nearly matching that of commercial 20 wt% Pt/C, can be traced to a synergistic combination of its structural, morphological, and electrochemical properties. At the core of its efficiency lies the unique interconnected porous network of J-800, which incorporates a hierarchical pore structure with micro-, meso-, and macropores [19]. This multiscale porosity is crucial as it increases the overall surface area and facilitates

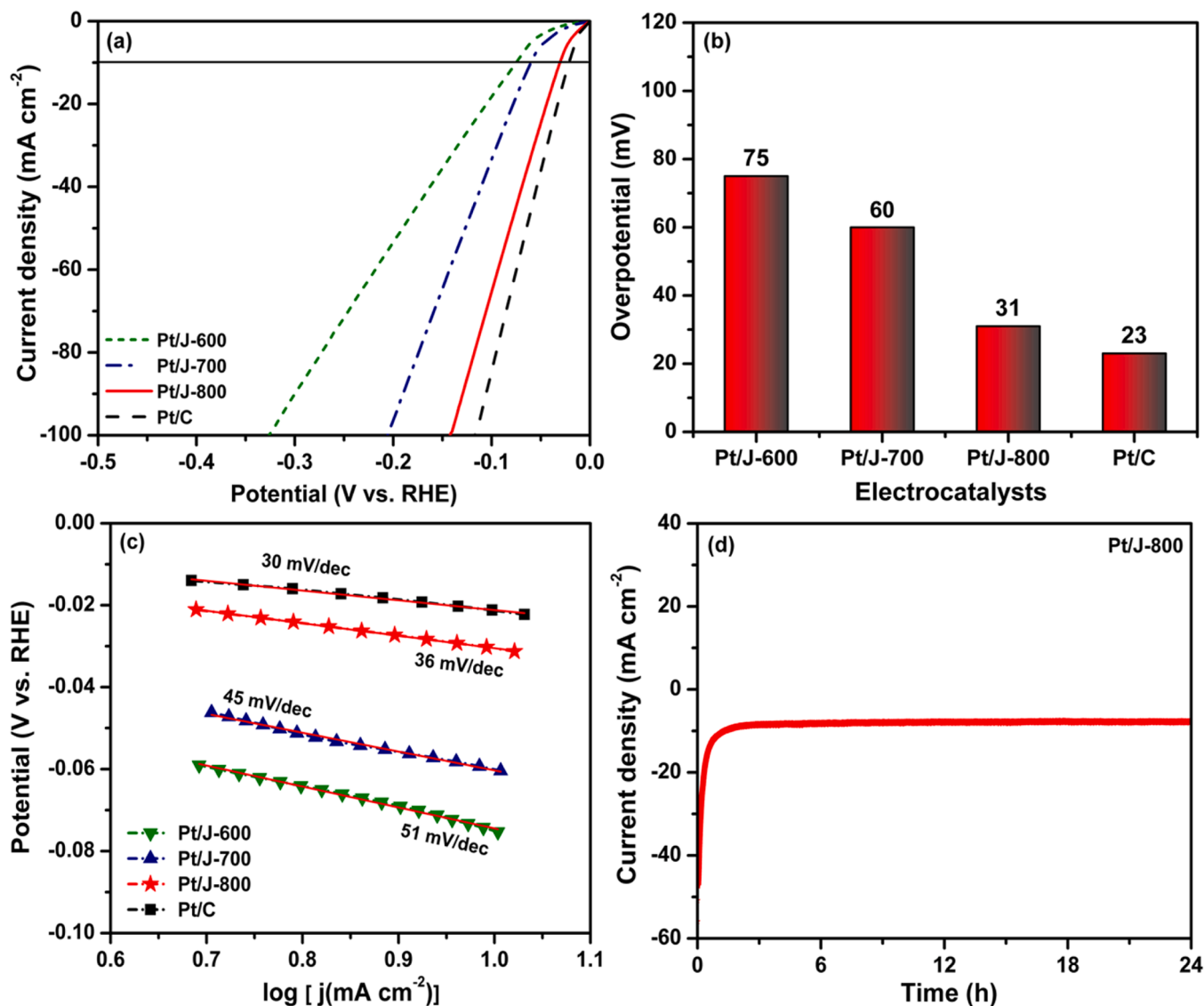


Fig. 9. a) LSV polarization curves for HER reaction, b) bar diagram on overpotentials of individual electrocatalysts at 10 mA cm^{-2} , c) Tafel Plot, and d) chronoamperometry of Pt/J-800.

efficient ion diffusion and electron transport, thereby minimizing mass transport limitations during catalytic reactions. The high Brunauer-Emmett-Teller (BET) surface area of J-800, an impressive $967 \text{ m}^2 \text{ g}^{-1}$ [19], significantly enhances the dispersion of Pt nanoparticles (NPs), preventing aggregation and ensuring a higher density of uniformly distributed active catalytic sites. The finely tuned dispersion of Pt NPs, with an average size of only 1.8 nm, contributes to a high surface-to-volume ratio, making many Pt active sites readily available for reactions such as the oxygen reduction reaction (ORR) and hydrogen evolution reaction (HER). Moreover, the hierarchical porosity supports not just the even dispersion of these nanoparticles but also enhances their accessibility to reactant molecules, boosting catalytic turnover and minimizing deactivation.

The structural defects in the carbon network of J-800, evidenced by its relatively high I_D/I_G ratio, further amplify its catalytic capabilities. These defects disrupt the sp^2 carbon conjugation, creating localized charged sites that act as additional catalytic centers, particularly beneficial in ORR, where these charged sites can lower the reaction overpotential [49]. This defective structure also enhances the overall electronic conductivity of J-800, enabling faster electron transfer between the Pt NPs and the electrode surface, a critical factor in

maintaining high catalytic activity. Coupled with this is the presence of surface functional groups such as hydroxyl and carbonyl on the J-800 support, which improve the hydrophilicity and wettability of the electrode. This increased wettability fosters better electrolyte contact, thereby reducing charge-transfer resistance and allowing for more efficient ion exchange at the catalyst-electrolyte interface. These functional groups also contribute to more effective diffusion of reactants to the active Pt sites, further accelerating reaction kinetics.

The synergy between the well-dispersed Pt NPs and the conductive J-800 support plays a central role in Pt/J-800's exceptional electrocatalytic performance. The ultra-small, uniformly distributed Pt NPs benefit from the enhanced electron transfer pathways provided by the highly conductive carbon matrix of J-800, resulting in significantly lower solution resistance, charge-transfer resistance, and diffusion resistance. This optimization of both electronic and ionic kinetics ensures faster charge transfer, reduced energy losses, and enhanced catalytic currents under operational conditions. Furthermore, the hierarchical porous structure optimizes mass and charge transport and contributes to the stability and durability of Pt/J-800 during prolonged operation. The porous network effectively mitigates nanoparticle agglomeration, a common cause of catalyst degradation, and resists

carbon corrosion, thus maintaining the structural integrity of the electrode under harsh electrocatalytic conditions.

Thus the superior performance of Pt/J-800 is a result of various interconnected factors such as high surface area, structural defects, uniform Pt NP dispersion, enhanced electron/ion transport, and strong electrode-electrolyte interactions. Together, they produce an electrocatalyst with exceptional electrocatalytic activity, rapid reaction kinetics, and long-term stability. The hierarchically porous carbon support not only provides a large, accessible surface area for electrocatalytic reactions but also ensures efficient charge and mass transfer. At the same time, the well-dispersed Pt NPs maximize the number of active sites. These synergies explain why Pt/J-800 exhibits such outstanding electrocatalytic performance, making it a promising candidate for applications in energy conversion and storage technologies, where both efficiency and durability are paramount.

4. Conclusions

Overall, a successful valorization of an environmentally malignant invasive weed into an efficient multifunctional electrocatalyst can be achieved through a simple hydrothermal carbonization technique followed by a controlled pyrolysis process. And the Pt loading is carried out using a facile polyol-mediated formaldehyde reduction process. XRD data reveals the highly turbostatic character of the carbon support, ensuring the proper anchoring site for Pt. Furthermore, the Raman I_D/I_G ratio validates the more defective structure of Pt/J-800. The TEM analysis illustrates the homogeneous dispersion of Pt NPs with an average particle size of 1.8 nm in Pt/J-800. The dotted ring-like concentric circles observed in the SAED pattern of Pt/J-800 confirm the highly poly-crystalline nature of loaded Pt NPs. The Pt/J-800 exhibits significantly lower resistance than other electrocatalysts prepared, implying high electronic conductivity. During RDE analysis, Pt/J-800 delivers a more positive onset potential (0.95 V_{RHE}), maximum half-wave potential (0.83 V_{RHE}), and a maximum limiting current density (-4.4 mA/cm^2). Moreover, the four-electron reduction pathway of Pt/J-800 is revealed through RRDE analysis. During methanol oxidation, Pt/J-800 provides a maximum ECSA ($49.09 \text{ m}^2 \text{ g}^{-1}$), higher forward peak current density (19.58 mA cm^{-2}), mass activity (652 A g^{-1}), and a large I_f/I_b ratio (2.10). While hydrogen evolution studies, Pt/J-800 demands a minimal overpotential (31 mV) and Tafel slope (36 mV/dec), validating the Volmer-Tafel reaction pathway during HER. In addition, the Pt/J-800 electrocatalyst displayed decay-free performance during the ORR (18 h), MOR (2 h), and HER durability tests (24 h).

CRediT authorship contribution statement

Sathyanarayanan Shanmugapriya: Writing – original draft, Investigation, Data curation, Conceptualization. **Mariappan Ganeshbabu:** Writing – original draft. **Subramani Surendran:** Writing – original draft, Formal analysis, Data curation, Conceptualization. **Yun Sung Lee:** Resources. **Ramakrishnan Kalai Selvan:** Writing – review & editing, Writing – original draft, Supervision, Conceptualization.

Declaration of competing interest

The authors declare that they have no known competing financial interests or personal relationships that could have appeared to influence the work reported in this paper.

The author is an Editorial Board Member/Editor-in-Chief/Associate Editor/Guest Editor for [Carbon Trends] and was not involved in the editorial review or the decision to publish this article.

Acknowledgment

Dr S. Shanmugapriya would like to acknowledge DST-PURSE, Phase-II Program, Bharathiar University, to provide a research fellowship.

Prof. Yun Sung Lee greatly acknowledged the National Research Foundation of Korea (NRF) grant funded by the Korean government (Ministry of Science, ICT & Future Planning) (No. RS-2023-00208361).

Data availability

Data will be made available on request.

References

- [1] A. Chalgin, C. Song, P. Tao, W. Shang, T. Deng, J. Wu, Effect of supporting materials on the electrocatalytic activity, stability and selectivity of noble metal-based catalysts for oxygen reduction and hydrogen evolution reactions, *Prog. Nat. Sci. Mater. Int.* 30 (2020) 289–297, <https://doi.org/10.1016/j.pnsc.2020.01.003>.
- [2] J. Barman, N. Deka, S. Rudra, G.K. Dutta, Promising N, P Co-doped Porous Carbon Materials as Metal-Free Electrocatalyst for Oxygen Reduction Reaction in Alkaline Medium, *ChemistrySelect* 7 (2022) e202200570, <https://doi.org/10.1002/slct.202200570>.
- [3] Y.W. Na, J.Y. Cheon, J.H. Kim, Y. Jung, K. Lee, J.S. Park, J.Y. Park, K.S. Song, S. B. Lee, T. Kim, S.J. Yang, All-in-one flexible supercapacitor with ultrastable performance under extreme load, *Sci. Adv.* 8 (2022) eabl8631, <https://doi.org/10.1126/sciadv.abl8631>.
- [4] R. Chen, H. Tang, P. He, W. Zhang, Y. Dai, W. Zong, F. Guo, G. He, X. Wang, Interface Engineering of Biomass-Derived Carbon used as Ultrahigh-Energy-Density and Practical Mass-Loading Supercapacitor Electrodes, *Adv. Funct. Mater.* 33 (2023) 2212078, <https://doi.org/10.1002/adfm.202212078>.
- [5] W. Yao, Y. Zhao, R. Chen, M. Wang, W. Song, D. Yu, Emissions of Toxic Substances from Biomass Burning: A Review of Methods and Technical Influencing Factors, *Processes* 11 (2023) 853, <https://doi.org/10.3390/pr11030853>.
- [6] M. Borghei, J. Lehtonen, L. Liu, O.J. Rojas, Advanced Biomass-Derived Electrocatalysts for the Oxygen Reduction Reaction, *Adv. Mater.* 30 (2018) 1703691, <https://doi.org/10.1002/adma.201703691>.
- [7] V. Dhyani, T. Bhaskar, A comprehensive review on the pyrolysis of lignocellulosic biomass, *Renew. Energy* 129 (2018) 695–716, <https://doi.org/10.1016/j.renene.2017.04.035>.
- [8] A. Sun, Y. Liu, J. Ma, L. Yang, Y. Wang, Preparation and oxygen reduction performance of nitrogen-doped cotton stalk-derived carbon, *Int. J. Low-Carbon Technol.* 17 (2022) 1029–1035, <https://doi.org/10.1093/ijlct/ctac067>.
- [9] G. Zhong, Z. Meng, M. Xu, H. Xie, S. Xu, X. Fu, W. Liao, S. Zheng, Y. Xu, Self-nitrogen-doped porous carbon prepared via pyrolysis of zhang-blade without additive for oxygen reduction reaction, *Diam. Relat. Mater.* 121 (2022) 108742, <https://doi.org/10.1016/j.diamond.2021.108742>.
- [10] J. Wang, D. Fan, L. Zhang, D. Yang, X. Qiu, X. Lin, Lignin-derived hierarchical porous carbon with high surface area and interconnected pores for efficient antibiotics adsorption, *Chem. Eng. J.* 454 (2023) 139789, <https://doi.org/10.1016/j.cej.2022.139789>.
- [11] D. Schonvogel, M. Nowotny, T. Woriescheck, H. Mulhaupt, P. Wagner, A. Dyck, C. Agert, M. Wark, Hydrothermal Carbonization-Derived Carbon from Waste Biomass as Renewable Pt Support for Fuel Cell Applications: role of Carbon Activation, *Energy Technol.* 7 (2019) 1900344, <https://doi.org/10.1002/ente.201900344>.
- [12] Z. Yang, C. Yan, M. Xiang, Y. Shi, M. Ding, J. Hui, Biomass carbon dual-doped with iron and nitrogen for high-performance electrocatalyst in water splitting, *Int. J. Energy Res.* 45 (2021) 8474–8483, <https://doi.org/10.1002/er.6381>.
- [13] V.C. Hoang, V.G. Gomes, K.N. Dinh, Ni- and P-doped carbon from waste biomass: a sustainable multifunctional electrode for oxygen reduction, oxygen evolution and hydrogen evolution reactions, *Electrochim. Acta* 314 (2019) 49–60, <https://doi.org/10.1016/j.electacta.2019.05.053>.
- [14] H. Yabu, K. Ishibashi, M.S. Grewal, Y. Matsuo, N. Shoji, K. Ito, Bifunctional rare metal-free electrocatalysts synthesized entirely from biomass resources, *Sci. Technol. Adv. Mater.* 23 (2022) 31–40, <https://doi.org/10.1080/14686996.2021.2020597>.
- [15] G. Li, J. Sha, L. Sun, R. Jin, T. Fu, Y. Xiang, Y. Tang, Y. Lei, Y. Si, C. Guo, Biomass coffee grounds derived nitrogen-doped ultrafine carbon nanoparticles as an efficient electrocatalyst to oxygen reduction reaction, *J. Alloys Compd.* 920 (2022) 165895, <https://doi.org/10.1016/j.jallcom.2022.165895>.
- [16] G. Gayathri, K.B. Uppuluri, The comprehensive characterization of Prosopis juliflora pods as a potential bioenergy feedstock, *Sci. Rep.* 12 (2022) 18586, <https://doi.org/10.1038/s41598-022-22482-9>.
- [17] K. Vignesh, M. Ganeshbabu, N.P. Naga, T. Mathivanan, B. Ramkumar, Y. Sung, R. K. Selvan, Oxygen-rich functionalized porous carbon by KMnO_4 activation on pods of Prosopis juliflora for symmetric supercapacitors, *J. Energy Storage* 72 (2023) 108216, <https://doi.org/10.1016/j.est.2023.108216>.
- [18] R.K. Sawal, R. Ratan, S.B.S. Yadav, Mesquite (Prosopis juliflora) Pods as a Feed Resource for Livestock – A Review -, *Asian-Australasian J. Anim. Sci.* 17 (2004) 719–725, <https://doi.org/10.5713/ajas.2004.719>.
- [19] S. Shanmugapriya, S. Surendran, Y.S. Lee, R.K. Selvan, Improved surface charge storage properties of Prosopis juliflora (pods) derived onion-like porous carbon through redox-mediated reactions for electric double layer capacitors, *Appl. Surf. Sci.* 492 (2019) 896–908, <https://doi.org/10.1016/j.apsusc.2019.06.147>.
- [20] S. Shanmugapriya, P. Zhu, C. Yan, A.M. Asiri, X. Zhang, R.K. Selvan, Multifunctional High-Performance Electrocatalytic Properties of Nb_2O_5

- Incorporated Carbon Nanofibers as Pt Support Catalyst, *Adv. Mater. Interfaces*. 6 (2019) 1–15, <https://doi.org/10.1002/admi.201900565>.
- [21] S. Shanmugapriya, P.R. Kasturi, P. Zhu, J. Zhu, C. Yan, X. Zhang, R.K. Selvan, Hexanedioic acid mediated in situ functionalization of interconnected graphitic 3D carbon nanofibers as Pt support for trifunctional electrocatalysts, *Sustain. Energy Fuels*. 4 (2020) 2808–2822, <https://doi.org/10.1039/d0se00136h>.
- [22] P. Rupakasturi, R. Kalai Selvan, Y.S. Lee, Pt decorated Artocarpus heterophyllus seed derived carbon as an anode catalyst for DMFC, *RSC Adv* 6 (2016) 62680–62694, <https://doi.org/10.1039/C6RA05833G>.
- [23] A. Jiang, B. Zhang, Y. Xue, Y. Cheng, Z. Li, Pt electrocatalyst supported on metal ion-templated hierarchical porous nitrogen-doped carbon from chitosan for methanol electrooxidation, *Microporous Mesoporous Mater* 248 (2017) 99–107, <https://doi.org/10.1016/j.micromeso.2017.04.025>.
- [24] Y. Fan, P. Liu, Z. Yang, T. Jiang, K. Yao, R. Han, X. Huo, Y. Xiong, Bi-functional porous carbon spheres derived from pectin as electrode material for supercapacitors and support material for Pt nanowires towards electrocatalytic methanol and ethanol oxidation, *Electrochim. Acta*. 163 (2015) 140–148, <https://doi.org/10.1016/j.electacta.2015.02.157>.
- [25] B. Tang, Y. Lin, Z. Xing, Y. Duan, S. Pan, Y. Dai, J. Yu, J. Zou, Porous coral reefs-like MoS₂/nitrogen-doped bio-carbon as an excellent Pt support / co-catalyst with promising catalytic activity and CO-tolerance for methanol oxidation reaction, *Electrochim. Acta*. 246 (2017) 517–527, <https://doi.org/10.1016/j.electacta.2017.06.052>.
- [26] J. Soddipinta, C. Ieasakulrat, N. Poonyayant, P. Kidkhunthod, N. Chanlek, T. Amornsakchai, P. Pakawatpanurut, Interconnected open-channel carbon nanosheets derived from pineapple leaf fiber as a sustainable active material for supercapacitors, *Ind. Crop. Prod.* 104 (2017) 13–20, <https://doi.org/10.1016/j.indcrop.2017.04.015>.
- [27] M. Geethalakshmi, M. Ganeshababu, S. Surendran, A. Stephen, Designing methanol tolerant Pt islands at Pd on carbon promoting electrocatalytic oxygen reduction reaction in acidic media, *Ionics* (Kiel) 28 (2022) 1347–1357, <https://doi.org/10.1007/s11581-021-04411-4>.
- [28] R. Ding, L. Lin, C. Pei, X. Yu, Q. Sun, H.S. Park, Hierarchical Architectures Based on Ru Nanoparticles/Oxygen-Rich-Carbon Nanotubes for Efficient Hydrogen Evolution, *Chem. - A Eur. J.* 27 (2021) 11150–11157, <https://doi.org/10.1002/chem.202101108>.
- [29] L. Qin, W. Lv, W. Wei, F. Kang, D. Zhai, Q.H. Yang, Oxygen-enriched carbon nanotubes as a bifunctional catalyst promote the oxygen reduction/evolution reactions in Li-O₂ batteries, *Carbon N. Y.* 141 (2019) 561–567, <https://doi.org/10.1016/j.carbon.2018.10.025>.
- [30] M. Dhelipan, A. Arunchander, A.K. Sahu, D. Kalpana, Activated carbon from orange peels as supercapacitor electrode and catalyst support for oxygen reduction reaction in proton exchange membrane fuel cell, *J. Saudi Chem. Soc.* 21 (2017) 487–494, <https://doi.org/10.1016/j.jscs.2016.12.003>.
- [31] G. Chen, H. Yang, Electrochemical Study of Oxygen Reduction Reaction on Natural Chalcopyrite in Sulfuric Acid and Ferric Solutions, *Int. J. Electrochem. Sci.* 11 (2016) 34–44, [https://doi.org/10.1016/S1452-3981\(23\)15824-X](https://doi.org/10.1016/S1452-3981(23)15824-X).
- [32] G. Montserrat-Sisó, B. Wickman, PdNi thin films for hydrogen oxidation reaction and oxygen reduction reaction in alkaline media, *Electrochim. Acta*. 420 (2022) 140425, <https://doi.org/10.1016/j.electacta.2022.140425>.
- [33] E. Marra, H. Grimler, G. Montserrat-Sisó, R. Wremland Lindström, B. Wickman, G. Lindbergh, C. Lagergren, Oxygen reduction reaction kinetics on a Pt thin layer electrode in AEMFC, *Electrochim. Acta*. 435 (2022) 141376, <https://doi.org/10.1016/j.electacta.2022.141376>.
- [34] L. Khotseng, Oxygen Oxygen Reduction Reduction Reaction Reaction, *Electrocatalysts for Fuel Cells and Hydrogen Evolution - Theory to Design*, IntechOpen, 2018, <https://doi.org/10.5772/intechopen.79098>.
- [35] S. Shoaib, A. Shah, T. Najam, C. Molochas, M.A. Nazir, A. Brouzgou, M.S. Javed, A. Rehman, P. Tsiakaras, Nanostructure Engineering of Metal – Organic Derived Frameworks : cobalt Phosphide Embedded in Carbon Nanotubes as an Efficient ORR Catalyst, *Molecules* 26 (2021) 6672, <https://doi.org/10.3390/molecules26216672>.
- [36] X. Wen, J. Miao, D. Mandler, M. Long, Rotating ring-disk electrode method to evaluate performance of electrocatalysts in hydrogen peroxide activation via rapid detection of hydroxyl radicals, *Chem. Eng. J.* 454 (2023) 140312, <https://doi.org/10.1016/j.cej.2022.140312>.
- [37] P. Varathan, S. Akula, P. Moni, A.K. Sahu, Natural aloe vera derived Pt supported N-doped porous carbon: a highly durable cathode catalyst of PEM fuel cell, *Int. J. Hydrogen Energy*. 45 (2020) 19267–19279, <https://doi.org/10.1016/j.ijhydene.2020.05.056>.
- [38] P. Dhanasekaran, A. Shukla, K.N. Krishnan, I. Rongrin, S.V. Selvaganesh, D. Kalpana, S.D. Bhat, Enhancing stability and efficiency of oxygen reduction reaction in polymer electrolyte fuel cells with high surface area mesoporous carbon synthesized from spent mushroom compost, *Sustain. Energy Fuels*. 3 (2019) 1012–1023, <https://doi.org/10.1039/C8SE00520F>.
- [39] P.R. Kasturi, S. Shanmugapriya, M. Elizabeth, K. Athira, R.K. Selvan, Electrocatalytic hydrogen evolution reaction studies of NiW_{1-x}Mo_xO₄ (x = 0.0, 0.5 and 1.0) nanoparticles in both acid and alkaline electrolytes, *J. Mater. Sci. Mater. Electron.* 31 (2020) 2378–2387, <https://doi.org/10.1007/s10854-019-02773-0>.
- [40] T. Zhou, H. Wang, S. Ji, V. Linkov, R. Wang, Soybean-derived mesoporous carbon as an effective catalyst support for electrooxidation of methanol, *J. Power Sources*. 248 (2014) 427–433, <https://doi.org/10.1016/j.jpowsour.2013.09.108>.
- [41] T. Zhou, H. Wang, S. Ji, H. Feng, R. Wang, Synthesis of Mesoporous Carbon from Okara and Application as Electrocatalyst Support, *Fuel Cells* 14 (2014) 296–302, <https://doi.org/10.1002/fuce.201300089>.
- [42] M. Sevilla, C. Sanchis, T. Valdés-solís, E. Morallón, A.B. Fuentes, Highly dispersed platinum nanoparticles on carbon nanocoils and their electrocatalytic performance for fuel cell reactions, *Electrochim. Acta*. 54 (2009) 2234–2238, <https://doi.org/10.1016/j.electacta.2008.10.042>.
- [43] X. Zhao, J. Zhu, L. Liang, C. Li, C. Liu, Biomass-derived N-doped carbon and its application in electrocatalysis, *Applied Catal. B, Environ* 154–155 (2014) 177–182, <https://doi.org/10.1016/j.apcatb.2014.02.027>.
- [44] N. Lobos, J. Manuel, V. Comignani, Biochar from pyrolysis of cellulose : an alternative catalyst support for the electro-oxidation of methanol ScienceDirect Biochar from pyrolysis of cellulose : an alternative catalyst support for the electro-oxidation of methanol, *Int. J. Hydrogen Energy*. 41 (2016) 10695–10706, <https://doi.org/10.1016/j.ijhydene.2016.04.041>.
- [45] N. Dubouis, A. Grimaud, The hydrogen evolution reaction : from material to interfacial descriptors, *Chem. Sci.* 10 (2019) 9165–9181, <https://doi.org/10.1039/c9sc03831k>.
- [46] N. Cheng, S. Stambula, D. Wang, M.N. Banis, J. Liu, A. Riese, B. Xiao, R. Li, T. Sham, L. Liu, G.A. Botton, X. Sun, Platinum single-atom and cluster catalysis of the hydrogen evolution reaction, *Nat. Commun.* 7 (2016) 13638, <https://doi.org/10.1038/ncomms13638>.
- [47] Q. Liu, Y. He, X. Weng, A. Wang, P. Yuan, K. Fang, J. Feng, One-pot aqueous fabrication of reduced graphene oxide supported porous PtAg alloy nanoflowers to greatly boost catalytic performances for oxygen reduction and hydrogen evolution, *J. Colloid Interface Sci.* 513 (2018) 455–463, <https://doi.org/10.1016/j.jcis.2017.11.026>.
- [48] T. Yang, M. Du, H. Zhu, M. Zhang, M. Zou, Immobilization of Pt Nanoparticles in Carbon Nano fibers : bifunctional Catalyst for Hydrogen Evolution and Electrochemical Sensor, *Electrochim. Acta*. 167 (2015) 48–54, <https://doi.org/10.1016/j.electacta.2015.03.077>.
- [49] J. C, X. Yi, Yi Jia, A Defect Electrocatalytic Mechanism: concept, Topological Structure and Perspective, *Mater. Chem. Front.* 2 (2018) 1250–1268, <https://doi.org/10.1039/C8QM00070K>.